2

Organic and Hybrid Solar Cells Based on Well-Defined Organic Semiconductors and Morphologies

Amaresh Mishra,[1] Volker Schmidt,[2] René A. J. Janssen,[3] and Peter Bäuerle[1]

[1] Institute of Organic Chemistry II and Advanced Materials, University of Ulm, Germany peter.baeuerle@uni-ulm.de
[2] Institute of Stochastics, Ulm University, Germany volker.schmidt@uni-ulm.de
[3] Molecular Materials and Nanosystems, Eindhoven University of Technology, The Netherlands r.a.j.janssen@tue.nl

Abstract. Organic and hybrid bulk-heterojunction solar cells are investigated. We describe the synthesis and solar cell characteristics of well-defined functional thiophene dendrimers. Three-dimensional morphologies of the polymer – metal oxide bulk heterojunctions are analysed with electron tomography and are analysed and simulated with stochastic models, to establish the effect of processing on morphology. Device models based using stochastically simulated data of morphologies and transport parameters are used to provide accurate description of solar cell performance.

2.1. Introduction

Polymer-based bulk heterojunction (BHJ) solar cells are considered as one of the most promising photovoltaic technologies in producing large-area and low-cost photovoltaic systems. The significant improvement in performance witnessed in recent years mainly resulted from a continuous development and improvement of new organic semiconducting materials that provide better overlap with the solar spectrum, higher charge carrier mobility, and improved film morphologies for charge generation, separation, and collection. Solar cells based on polymer-fullerene blends junctions have reached power conversion efficiencies (PCEs) over 10% recently [1].

In parallel to developing conjugated polymers for solar cell applications, interest in developing solution-processable small molecule-based solar cells is increasing over the last five years. In comparison to polymeric materials, small molecules have distinct advantages with respect to straightforward synthesis, defined structures and purity, which greatly improve fabrication reproducibility and avoid batch to batch variations. The best single junction solution-processed, small molecule-based solar cells also reach PCEs close to 10% [2].

It is widely accepted that the performance of organic solar cells critically depends on the three-dimensional (3D) nanomorphology of their photoactive layers, which is influenced by various process parameters. Presently the choice of appropriate process parameters required to balance phase separation for charge generation and, at the same time, for charge transport

is a challenging multi-parameter optimization problem, which is solved in a purely empirical way. This is unsatisfactory, but quantitative approaches based on a systematic understanding of the influence of 3D nanostructure on performance are widely missing. One reason for this situation is that the experimental determination of the 3D nanostructure of photoactive layers with two organic (donor-acceptor) semiconductors via electron tomography is hampered by the low contrast between the two organic phases.

Progress in PCE compared to the present state of the art is possible by further reducing energetic and recombination losses that presently limit the performance. For single junction solar cells pursuing two main goals, can be identified:

(1) Development of pure, well defined organic semiconductors
(2) Rational design of donor-acceptor morphologies

In this chapter we provide an overview of recent developments towards these goals, with an emphasis on results that were obtained in a collaborative research project of the authors, where chemistry, materials science, physics, and mathematics were combined to investigate organic solar cells based on blends of well-defined thiophene dendrimers with fullerenes, and hybrid solar cells based on π-conjugated polymers and metal oxides.

2.2 All-Thiophene Dendrimers

Functional oligothiophenes have attracted comprehensive attention among researchers all over the world and have actually been advanced to be among the most frequently used π-conjugated materials in particular as active components in organic electronic devices and molecular electronics [3]. Recently, the traditional linear π-conjugated oligothiophenes have been extended to three-dimensional dendritic and hyperbranched structures. In this respect, a multitude of various functional molecular architectures have been established and characterized.

Thiophene chemistry is well established and there are uncountable methods to modify the core molecule [4]. Most importantly, thiophenes are ideal building blocks in transition metal-catalysed cross-coupling reactions, which have been enormously developed in the past decades and nowadays provide the basis for the synthesis of the great variety of conjugated π-systems. Oligothiophene-based materials possess outstanding chemical and physical properties and their electronic properties can be tuned by enormous structural variations. They are typically stable in various oxidation states and can be readily characterized by many methods. Their unique electronic, optical, and redox properties are intriguing, as well as their unique self-assembling properties on solid surfaces or in the bulk. Finally, the high polarizability of sulphur atoms in thiophene rings leads to a stabilization of the conjugated chain and to excellent charge transport properties which are one of the most crucial assets for applications in organic and molecular electronics.

Three-dimensional branched architectures, generally termed as dendrimers, represent a class of synthetic macromolecules that have dramatically impacted the field of organic and polymer chemistry and created a new branch in synthetic and material chemistry. These dendritic macromolecules can be synthesized by either divergent or convergent approaches. The divergent method comprises sequential addition of building blocks or repeating units to

the central multi-functional core. The built-up of the dendrimers goes towards the periphery by protection and deprotection techniques. In contrast, in the convergent method the building blocks are first constructed step-wise with different generations and are then attached to a specific functional core unit. Functionalization of dendrimers with oligothiophenes at the core or periphery as well as purely thiophene-based dendrimers was materialized just recently.

2.2.1 Thiophene Dendrimers Functionalized at the Periphery

Over the past years, a variety of dendrimers have been constructed with different core, periphery and branching units, with flexible and rigid structures. Conjugated, rigid and shape-persistent dendritic structures were constructed comprising phenylacetylene [5,6], phenylene-vinylene [7], or exclusively phenylene units or phenylene-thiophene systems [8,9]. Purely thiophene-based dendrimers and dendrimers with oligothiophenes at the core or periphery are of a more recent date. The first examples of *all*-thiophene dendrimers were reported by Advincula *et al.* in 2002 [10]. They synthesized dendritic oligothiophenes consisting of 30 thiophene units (up to a 3rd generation (*G3*), Fig. 2.1) by a convergent approach using transition metal-catalysed Kumada- and Stille-type couplings. The primary building block used was a *α,β*-branched terthiophene, in which hexyl side chains are attached at the periphery to improve solubility in common organic solvents.

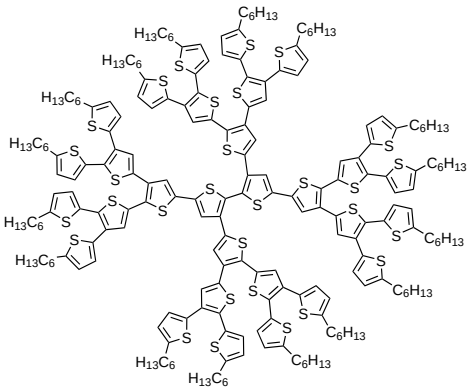

Fig. 2.1. 3rd Generation *all*-thiophene dendrimers reported by Advincula *et al.* [10]

The Bäuerle group recently developed an effective approach to novel functionalized dendritic oligothiophenes (DOTs) with the aim to create 3D semiconducting materials, which can be further functionalized at the periphery with, e.g., dyes, redox active, self-organizing or biological groups. These functional dendrons can also be easily attached to core structures of interesting geometric and electronic properties. As basic building block trimethylsilyl (TMS)-protected branched 2,2':3',2"-terthiophene was used to directly allow selective reactions at the free α-position to build up higher generational DOTs [11]. In contrast to the system developed by Advincula, in our case, the TMS-protecting groups allowed further transformations at the other *α*-positions and can either be cleaved off to give the “pure” oligothiophenes or be converted to other functional groups by electrophilic *ipso*-reactions.

Via repetition of the sequential divergent-convergent synthetic protocols, the first series of protected and non-substituted DOTs up to the 4th generation (*G4*) were synthesized. The *G*4

dendron **45T** and dendrimer **90T** are monodisperse and highly soluble in common organic solvents (Fig. 2.2).

The UV-Vis absorption profiles of the dendrimers with different generations measured in dichloromethane are shown in Fig. 2.3. All these thiophene dendrimers showed intense broad and structureless absorption spectra covering 300-550 nm. With increasing generation the molar extinction coefficient increases and the optical energy gaps (E_g) decrease from 2.5 eV to 2.2 eV and are within the range of linear semiconducting oligo- and polythiophenes [11,12,13]. In these dendritic systems the absorption profile revealed conjugation paths along the α-β connections of the chromophoric subunits. It has also been shown that the absorption spectra were a superimposition of multiple chromophores, which correlate to α-conjugated oligothiophene subunits. Emission typically came from the longest chromophoric α-conjugated pathway and was invariant to the excitation wavelength. This behaviour, together with the very low fluorescence quantum yields, clearly indicated intramolecular energy transfer from shorter chromophores to the longest one, which then emits in these systems.

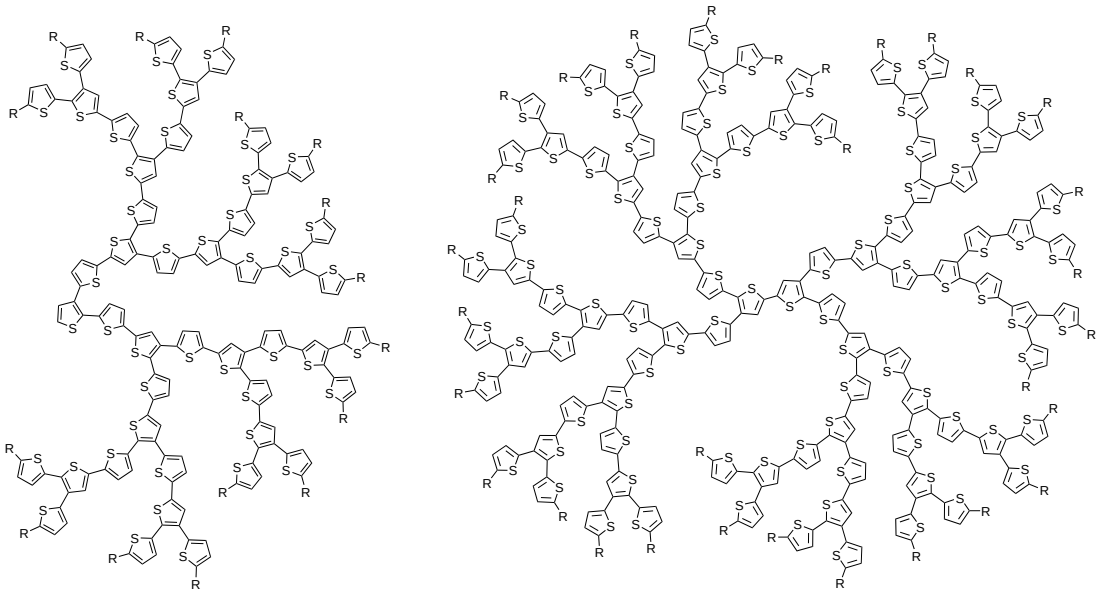

Fig. 2.2. Structures of dendron with 45 thiophenes and dendrimer with 90 thiophenes

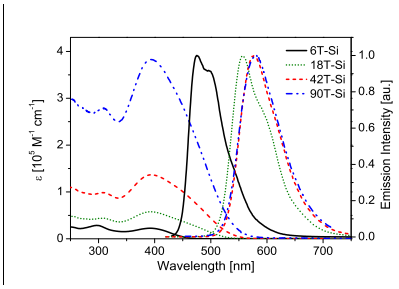

Fig. 2.3. Optical absorption and emission spectra of dendritic oligothiophenes with increasing generation. 6T-Si = *G*1; 18T-Si = *G*2; 42T-Si = *G*3; and 90T-Si = *G*4 (*G* = generation)

Solution processed bulk-heterojunction solar cells were fabricated (device architecture ITO/PEDOT: PSS/DOT:$PC_{61}BM$/LiF/Al) using these dendrimers as donor materials in combination with $PC_{61}BM$ ([6,6]-phenyl-C_{61}-butyric acid methyl ester) as acceptor [12]. BHJ solar cells for dendrimer **D1** (R= H) (Fig. 2.4) in a D-A ratio of 1:2 generated a PCE of 1.7% with a high V_{OC} of 0.97 V and J_{SC} 4.19 mA cm^{-2}. It is also important to note that for optimal performance the number of thiophene units in these monodispersed dendritic oligothiophenes per $PC_{61}BM$ is about 5-6 units. Tapping mode AFM investigation on the BHJ layers revealed smooth surfaces for the different generations with nanoscale phase separation of the dendrimer and the $PC_{61}BM$ [12].

The hole mobility of around 10^{-5} cm^2 V^{-1} s^{-1} for these pristine dendrons and dendrimers with 21 or 42 thiophene units measured by charge extraction by linearly increasing voltage technique (CELIV) was found to be relatively invariant indicating that shape and size of the studied dendrimers have little influence on their charge transport properties. The hole mobility was decreased by a factor of 3-10 for the TMS-protected molecules which was attributed to the insulating effect of the peripheral TMS-groups reducing charge transfer rates between neighbouring dendritic molecules. The decreased hole mobility in the blend and a rather short charge carrier lifetime measured by photo CELIV are thought to be the limiting factors for overall power conversion efficiency in these devices [14].

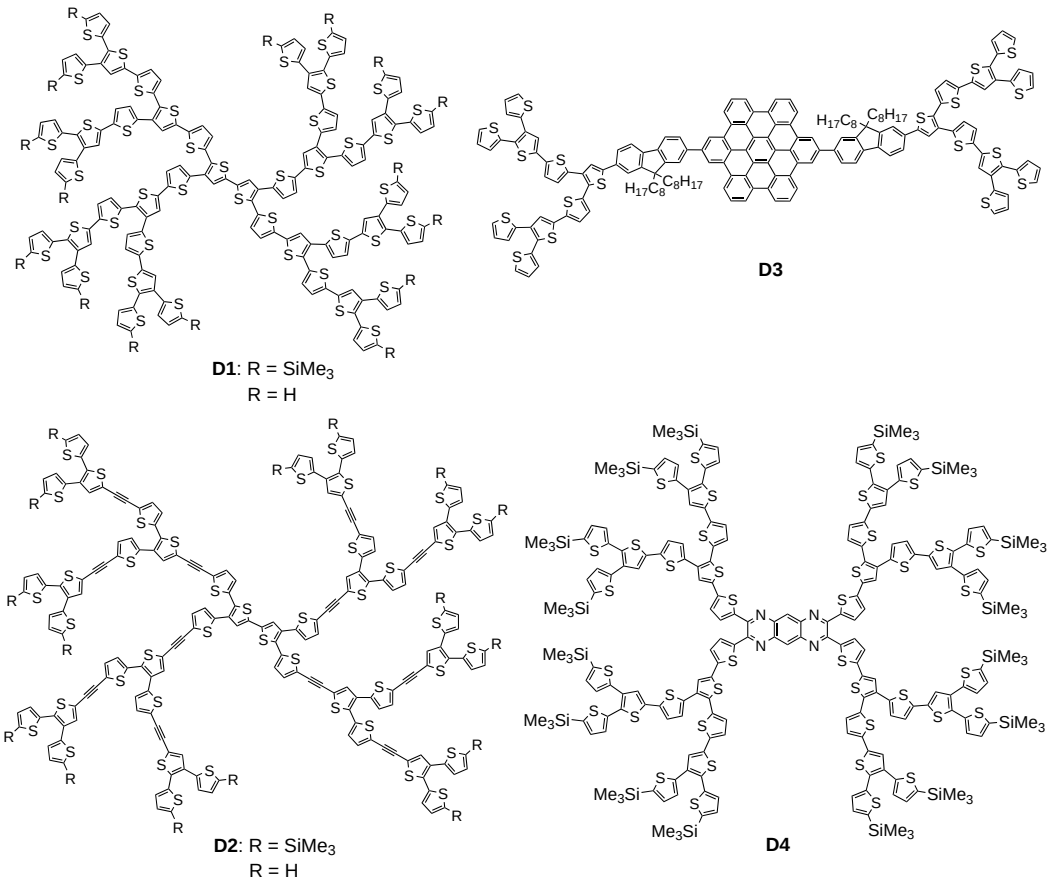

Fig. 2.4. Structures of **D1**, **D2**, **D3** and **D4**

2.2.2 Thiophene Dendrimers Functionalized in the Branches or at the Core

We have also functionalized the dendrimers by introduction of ethynyl units in the branching points. Investigations of the optical properties revealed that, in comparison to *all*-thiophene dendrimer **D1**, the introduction of ethynyl groups in the branching units in **D2** caused a hypsochromic shift of the low energy absorption band (Fig. 2.4) [15]. The HOMO energy levels of **D2** (R = $SiMe_3$) comprising ethynyl units was around -5.6 eV, which is about 0.3 eV lower compared to **D1** (R = $SiMe_3$) (-5.3 eV). BHJ solar cells were prepared with dendrimer **D2** (R = $SiMe_3$) as donor and $PC_{61}BM$ as acceptor in a D:A blend ration of 1:4 giving rise to a PCE of 0.4% and a V_{OC} of 0.81 V. In a similar D:A ratio dendrimer **D1** (R = $SiMe_3$) generated a higher PCE of 1.0% due to higher J_{SC} and V_{OC} values. The lower J_{SC} for the device based on ethynylated dendrimer **D2** compared to **D1** could be due to unbalanced charge carrier mobility of the former, which was also reflected in the lower EQE value of 17% for **D2** compared to 45% for **D1**.

Wong *et al.* and us synthesized a series of hexa-*peri*-hexabenzocoronene (HBC) derivatives comprising dioctylfluorenyl moieties end-capped with oligothiophene dendrons and implemented as donor material in the active layer of BHJ solar cells [16]. The HBC derivatives showed self-association behaviour into ordered structures in solution and in the solid state. BHJ solar cells fabricated using HBC derivative **D3** (Fig. 2.4) as electron donor and $PC_{61}BM$ as electron acceptor (1:2, w/w) gave PCEs of up to 1.5%. This study clearly demonstrated the positive effect of molecular self-organization in the solid state on device performance. The PCE of devices based on **D3** was further increased to 2.5% by using $PC_{71}BM$ ([6,6]-phenyl-C_{71}-butyric acid methyl ester) as acceptor due to an increase of the J_{SC} value to 6.4 mA cm^{-2}.

In order to extend the absorption range of DOTs, we introduced a strong electron-accepting pyrazino[2,3-*g*]quinoxaline core into the dendritic structure in **D4** (Fig. 2.4) [17]. Compared to thiophene dendrimer **D1**, **D4** showed a broad absorption band covering 300-700 nm and a reduced band gap of 1.7 eV. In BHJ solar cells, low band gap dendrimer **D4** gave a PCE of 1.3% in combination with $PC_{61}BM$ as acceptor whereas a PCE of 1.0% was obtained with all-thiophene dendrimer **D1** (R = $SiMe_3$). Using $PC_{71}BM$ as acceptor, devices based on **D4** gave a PCE of 1.7% and a high open circuit voltage (V_{OC}) of 0.98 V. This study showed that the longest wavelength intramolecular charge-transfer band contributes to the external quantum efficiency (EQE) spectrum, which was extended up to 750 nm, and consequently to the photocurrent. Recently, desilylated dendron **D4** containing a pyrazino[2,3-*g*]quinoxaline core was also synthesized exhibiting power conversion efficiencies of 0.9% by blending with $PC_{61}BM$ and 1.6% with $PC_{71}BM$ as acceptor, respectively [18].

Furthermore, dendrons were functionalized with pyridinium units. For example, dendron **D5** (Fig. 2.5) showed absorption bands at 390 and 535 nm which were assigned to the oligothiophenes dendron and to the corresponding charge transfer absorption arising from the oligothiophene donor and pyridinium acceptor, respectively [19]. A pyridine unit was used to form complexes with phthalocyanines (Pc) as it was realized in the case of **D6** (Fig. 2.5) [20]. It has been shown that the absorption band of the Pc-dendron complexes increased at higher energies when the dendron generation increased. However, the HOMO energies (~-5.1 eV) were found to be independent of the dendron size. Implementation of the functional dendrons **D5** and **D6** in BHJ solar cells generated PCEs 0.45 and 0.7%, respectively, in combination with $PC_{61}BM$ as acceptor. The devices based on Pcs, which comprise a 3T-dendron, gave PCEs of 1.0% with $PC_{61}BM$ and 1.5% with $PC_{71}BM$ as acceptor. The contribution of the Pc core in the

photocurrent generation, about 40%@630 nm, can be clearly seen in the EQE) spectrum which corresponds to the absorption band of the Pc unit.

Ma and co-workers synthesized a dendron functionalized with squaraine dye **D7** (Fig. 2.5), which showed strong absorption at around 680 nm and a HOMO energy level in the range of -5.11 to -5.16 eV. The band gap of dendrimer **D7** determined by cyclic voltammetry was 1.73 eV. In planar-heterojunction solar cells PCEs up to 1.6% have been measured at low light condition (50 mW cm^{-2}).

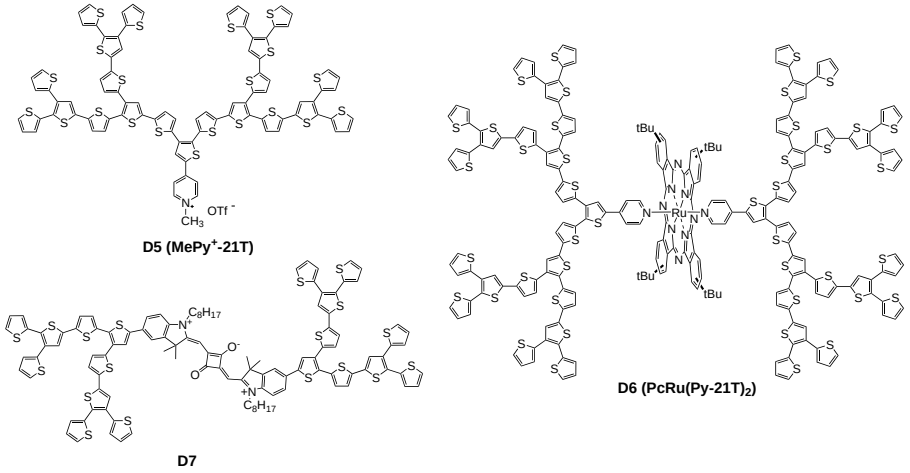

Fig. 2.5. Structures of **D5**, **D6** and **D7**

2.2.4 Thiophene Dendrimers with Extended Branches

Zhang designed and synthesized dendron **D8** and dendrimer **D9** functionalized in the periphery with benzothiadiazole as acceptor units (Fig. 2.6) [21]. The absorption feature of these molecules showed two absorption bands – one at higher energy around 330 nm which is assigned to the π-π* transition and one at lower energy around 500 nm assigned to an intramolecular charge transfer (ICT) band. In comparison to solution spectra, a red-shift of 25 nm was observed in thin films. The optical energy gap for **D8** and **D9** was 2.1 and 2.03 eV in solution and 2.0 and 1.82 eV in thin films, respectively. The HOMO energy levels were determined to be about -5.6 and -5.3 eV, respectively. The devices (ITO/PEDOT:PSS/ DOT:$PC_{61}BM$ (1:3) (w/w)/LiF/Al) based on **D8** and **D9** as donor and $PC_{61}BM$ as acceptor gave high V_{OC} of up to 1.04 V, J_{SC} up to 3.7 mA cm^{-2}, and PCEs of 1.2% and 1.3%, respectively [21].

Insertion of additional thiophene units into the branches of a terthiophene dendron to prepare a quinquethiophene (5T)-dendron was further developed by Zhang [21]. She prepared higher generational dendrimers up to the 3rd generation (**D10**, **D11**, Fig. 2.7). The dendrimers were synthesized starting from a 5T-dendron following the similar synthetic strategies shown in Scheme 1 for the terthiophene-based dendrimers. Both, D10 and D11, showed a broad and structureless absorption band with a maximum at around 438 nm and an optical energy gap of 2.3 eV. BHJ solar cells prepared from these dendrons and dendrimers as donor and $PC_{71}BM$ as acceptor in a weight ratio of 1:3 generated high V_{OC}s of up to 0.95 V and PCEs of 2.2% and 3.1%, respectively. Dendron **D10** comprising 35 thiophene units showed an EQE maximum of 53% at 470 nm. Post-processing by thermal annealing or solvent additives did not lead to a further improvement of the device performance.

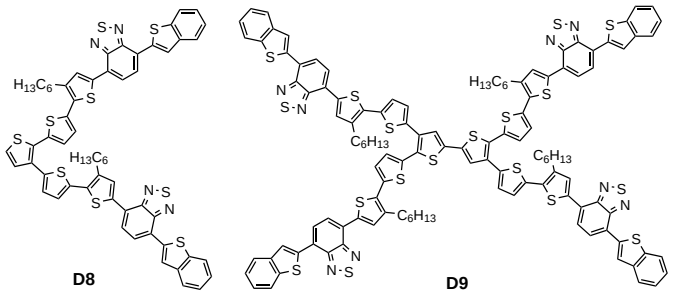

Fig. 2.6. Structures of **D8** and **D9**

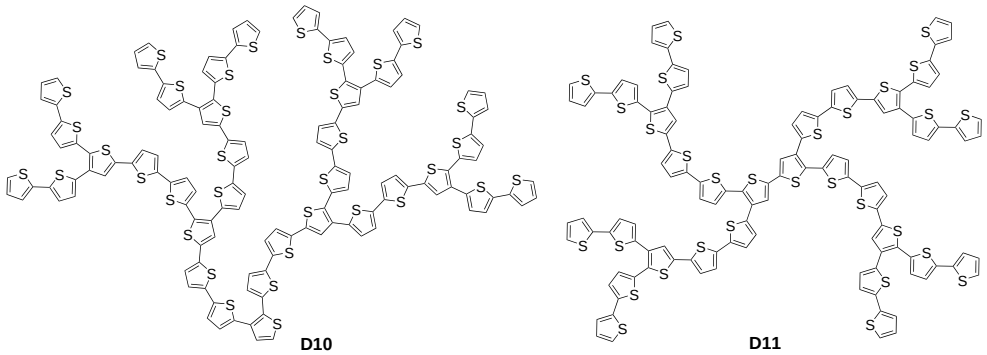

Fig. 2.7. Structures of **D10** and **D11**

2.3 Morphology and Performance of Hybrid and Polymer Solar Cells

The morphology of the photoactive layer in donor-acceptor bulk-heterojunction solar cells is undoubtedly one of the most crucial parameters in determining the photovoltaic performance. The size and extent of the phase separation determine the distance over which excitons have to travel to reach the donor-acceptor interface where they can be dissociated into charge carriers. As a result exciton dissociation is favoured when the two materials are intimately mixed. In contrast, charge separation involves diffusion and drift of holes and electrons away from the interface and benefits from delocalized wave functions in large semi-crystalline domains and is therefore favoured in phase separated blends. Finally, charge collection requires that holes and electrons move via unobstructed percolation pathways to the electrodes where the can be collected. This not only requires the presence of almost pure phases, but also the absence of cul-de-sacs in the morphology in which charges may be physically trapped. If charge separation or charge transport is sluggish, the photogenerated holes and electrons recombine via monomolecular (or geminate) and bimolecular recombination, resulting in a loss of photocurrent, fill factor and power conversion efficiency.

Koster *et al.* have developed a straightforward method to quantify the fraction of charge carriers that recombines bimolecularly under operating conditions [22]. The experimental technique is based on measuring the differential current density ΔJ induced by a small modulation in light intensity (ΔI) in the presence of a background light intensity I. This steady-state differential current technique easily resolves non-linear behaviour that is obscured in conventional J–I measurements and enables the direct experimental determination of

intensity dependent losses. Koster *et al.* also derived an analytical model to quantitatively relate these losses to bimolecular recombination [22]. This model offers a direct link between the bimolecular recombination loss efficiency (η_{BR}) and the intensity dependence of the short circuit current as $\eta_{BR} = \alpha^{-1} - 1$, where α is the exponent of the intensity (I) dependence of the short circuit current $J_{SC} \propto I^{\alpha}$. Remarkably, it was found that bimolecular losses in BHJ solar cells can amount to tens of % under solar illumination while J_{SC} vs. I seemingly remains linear.

To reach optimum performance, the typical domain size of phase-separated domains should be on the order of 10 nm as a compromise between efficient charge generation and collection. In reality the actual morphology is often hierarchical in nature in the sense that apart from pure phases also mixed domains exist and charge collection occurs via a network of short narrow filaments that interconnect larger domains, much like the artery system. The desired ~10 nm size of the features, presently precludes the use of top-down fabrication of the ideal morphology. Instead, morphology formation involves autonomous processes such as self-assembly, crystallization and phase separation using the natural tendency of polymers not to mix as a consequence of a low mixing entropy. In general, morphology formation from a solution of donor-acceptor materials is a non-equilibrium process that can occur within a fraction of a second, governed by the evaporation rate of the solvent. It is often assumed that the resulting morphology is a kinetically trapped state and that post-deposition techniques such as thermal or solvent vapour annealing result in thermodynamically more stable states.

Although the importance of morphology is very well recognized as a crucial parameter in organic solar cells, many questions and challenges remain. E.g. few techniques are available that allow determining the three-dimensional morphology on a nanoscale. If the morphology has been measured, is it then possible to predict the device performance with a suitable physical device model? A more daunting challenge is to rationalize the relation between processing conditions and the resulting morphology. In the next sections we address these is issues, for two examples polymer – metal oxide and polymer – fullerene blends.

2.3.1 Polymer – Metal Oxide Solar Cells

An elegant way of fabricating hybrid polymer – metal oxide solar cells is via depositing a semiconducting polymer and a metal oxide precursor from solution in which the precursor is converted by reacting with water from the ambient to form a metal oxide network inside the polymer. An example of this method is using poly(3-hexylthiophene) (P3HT) and diethyl zinc as precursor for ZnO. In this way it is possible to make P3HT:ZnO solar cells with a PCE of about 2% at an active layer thickness of 225 nm [23]. In these cells the external quantum efficiency (EQE) maximizes at 44 % at 520 nm.

Thicker P3HT:ZnO layers gave a higher internal quantum efficiency (IQE) than thin cells (Fig. 2.8). The number of photons absorbed by the P3HT:ZnO layer calculated by optical modelling of the entire stack of layers, revealed that the IQE (Fig. 2.8) increases significantly with layer thickness [23]. Hence, somewhat counterintuitively, in thicker layers, photons are also more efficiently transformed into collected charges. To understand this behaviour, we spatially resolved the morphology of P3HT:ZnO layers in the nanometre range using electron tomography (Fig. 2.9). ZnO provides good contrast with the polymer in electron microscopy, enabling a nanometre resolution. To quantify the effect of the coarseness of the experimental morphologies on the charge carrier generation of P3HT:ZnO solar cells, the exciton diffusion in the active layer has been modelled. The diffusion of excitons in the polymer phase was

described by the diffusion equation for excitons [23] in the experimentally determined morphologies. Fig. 2.9. shows the calculated exciton dissociation efficiency for different layer thicknesses and reveals that exciton dissociation is far more efficient in the thicker layers as a consequence of their finer morphology, giving a first explanation of why the IQE increase with layer thickness.

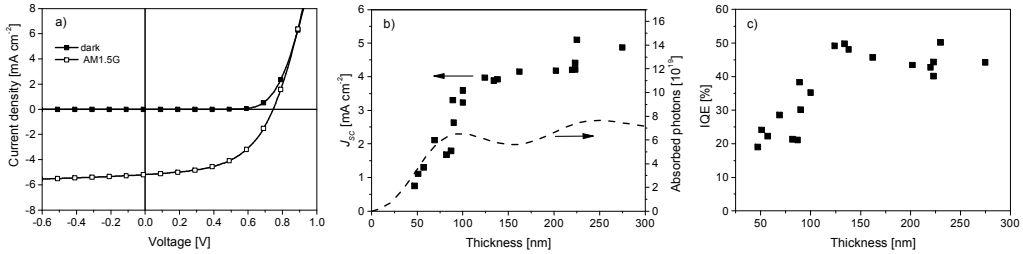

Fig. 2.8. Performance of P3HT:ZnO solar cells. (a) *J-V* characteristics. (b) *J* and absorbed photon flux vs. thickness. (c) IQE vs. thickness. The thickness was varied by altering the spin speed. Reprinted from [23] with permission from Nature Publishing Group

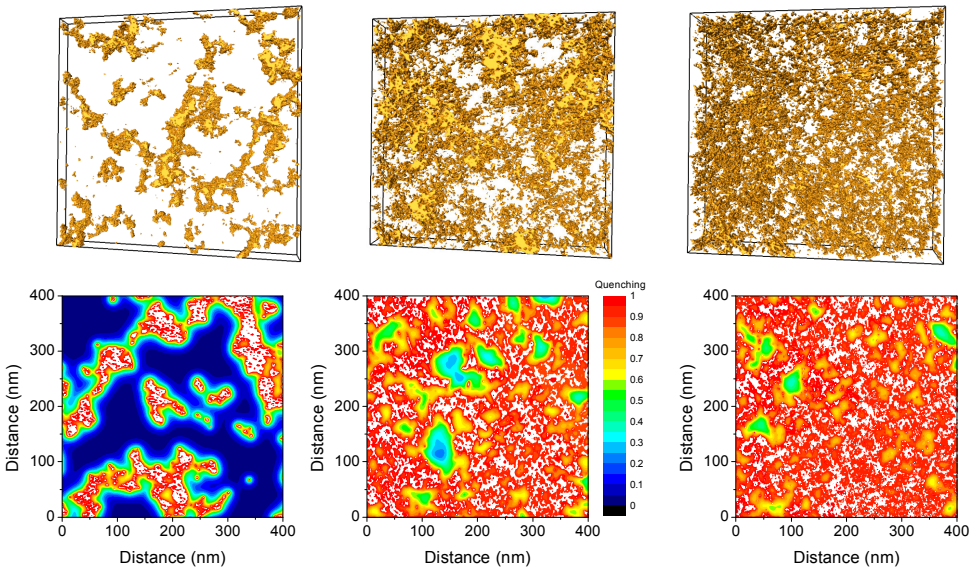

Fig. 2.9. Top row: Electron micrographs of typical P3HT:ZnO blends; from left to right thickness is 57, 100, and 167 nm. The size of all samples is 700 × 700 nm; ZnO appears yellow, P3HT transparent. Bottom row: Modelled exciton dissociation efficiency cross sections in the same blends. Reprinted from [23] with permission from Nature Publishing Group

While the influence of morphology on charge generation is relatively easy to model, charge transport in disordered donor-acceptor blends is more difficult to describe. In a first study, Koster has investigated the charge carrier mobility in disordered organic blends for photovoltaics theoretically by numerically solving the Pauli master equation [24]. He found that the well-known dependence of mobility on charge carrier concentration is even more pronounced in blends than in the pure materials and that it is influenced by the electric field strength. At low charge carrier densities in the blend, the mobility was found to decrease with

increasing field. For strongly disordered materials charge transport is favoured by relatively large domains.

In a subsequent study Koster combined optical and charge transport models to establish the relation between morphology and performance in more detail and create a quantitative link between efficiency and morphology using the experimental 3D morphology of P3HT:ZnO blends and a 3D optoelectronic device model [25]. This model includes the effects of exciton diffusion and dissociation; space-charge; recombination, generation, drift and diffusion of charge carriers; and the injection/extraction of carriers at the contacts. The observed trend in internal quantum efficiency as a function of layer thickness as shown in Fig. 2.8 was reproduced with a single set of parameters. The model reveals that isolated clusters of ZnO that are more than a few times the exciton diffusion length away from the main ZnO phase do not affect the overall device efficiency. The impact of cul-de-sacs, however, is more complex and depends on the local electric field and the depth of the cul-de-sac. This first direct use of morphological data in an optoelectronic device model shows that it is indeed possible to quantitatively link morphology to device performance.

In an attempt to control the morphology of conjugated polymer:ZnO solar cells by the chemical structure we have investigated the effect of side chain functionalization [26]. Using an ester-functionalized side chain poly(3-hexylthiophene-2,5-diyl) derivative (P3HT-E), the nanoscale morphology of polymer:ZnO solar cells is significantly more intimately mixed compared to P3HT:ZnO as evidenced experimentally from a 3D reconstruction of the phase separation using electron tomography and the modelling of the charge generation efficiency (Fig. 2.10). In the P3HT-E:ZnO blends nearly quantitative charge transfer occurs. For thin P3HT-E:ZnO active layers (~50 nm) this yields a significant improvement of the solar cell performance. For thicker cells, however, the reduced hole mobility and a reduced percolation of ZnO pathways hinders charge carrier collection, limiting the power conversion efficiency.

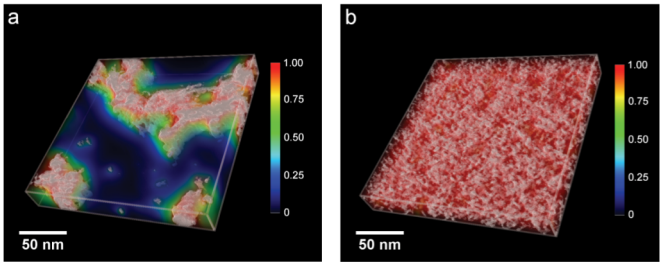

Fig. 2.10. Calculated charge carrier generation efficiency in experimentally determined morphologies for P3HT:ZnO (a) and P3HT-E:ZnO (b). The ZnO appears white; the efficiency is indicated by the colour. Reprinted from Ref. [26] with permission from Wiley

In summary, using a combination of electron tomography and electro-optical device modelling a coherent and consistent picture has emerged for the device physics of polymer – metal oxide solar cells in relation to the morphology. Although these cells are unable to compete in terms of device performance with the most efficient polymer-fullerene solar cells, the characteristics of these studies seem generally applicable. In section 2.4.1 we will come back to these P3HT:ZnO blends and describe a stochastic morphology model and a stochastic multiscale model that is then used to create virtual 3D microstructures for different processing conditions.

2.3.2 Polymer – Fullerene Solar Cells

The active layer morphology in polymer-fullerene blends has been extensively studied, but relatively little information is available on the active layer formation. Van Franeker et al. have recently developed in-situ optical techniques that allow to determine the active layer thickness, the formation of phase separation and the aggregation of polymer chains during spin coating with millisecond time resolution [27]. One of the interesting phenomena that quite often occurs during spin coating of the photoactive layer in polymer-fullerene blends is a process called liquid-liquid phase separation, which results in the formation of large droplet-like fullerene domains in a matrix that consists of polymer and fullerene. An example of this morphology is shown in Fig 2.11 for a mixture of a diketopyrrolopyrrole-quinquethiophene copolymer (PDPP5T) with $PC_{71}BM$ in a 1:2 weight ratio [28]. Depending on the spin rate and total concentration of polymer and fullerene, different sized domains can be obtained. Although these strongly phase separated morphologies are less relevant for efficient solar cells, and they be circumvented by the use of a co-solvent [27], it is important to understand their formation and the parameters that control length scales in phase-separated films, if we want to understand morphology formation from evaporating solvents in more detail. The droplet-like features are a consequence of spinodal demixing and we were interested in the parameters that determine the size of these domains. Thereto we analysed the drying process of spin coated inks that undergo liquid-liquid phase separation via determining the drying rate in the evaporation phase of the spin coating. Light scattering experiments showed that during this phase liquid-liquid demixing occurs. As such we were able to show that the size of these droplets scales with the normalized drying rate, i.e. the drying rate normalized to the final thickness of the film. The scaling is valid over two orders of magnitude and has been verified for several material combinations. The normalized drying rate can be related to two possible "determinants" of domains size: (1) the quench rate, which would determine length scales by the amplification of an initial length scale by spinodal decomposition (early-stage), or (2) to the coarsening time, in which the growth of already existing domains can take place (late-stage, for example Ostwald ripening).

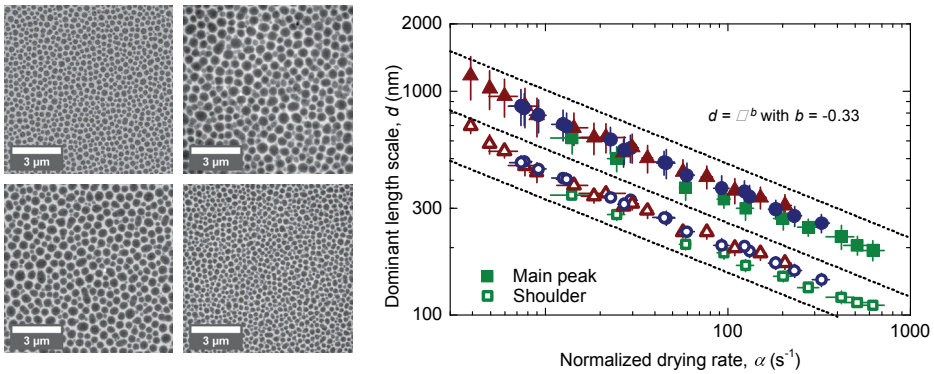

Fig. 2.11. Right: Examples of morphologies obtained for different total concentrations of polymer and fullerene in chloroform. Left: Relationship between the dominant length scale and normalized drying rate. Different initial polymer concentrations are indicated: green squares are 3 mg mL^{-1}, dark blue circles are 6 mg mL^{-1}, and dark red triangles are 9 mg mL^{-1}. The scaling law is valid for all concentrations. Solid symbols indicate the main peak position from the Fourier transform, while open symbols represent the location of a shoulder in the Fourier transform. Reprinted from Ref. [28] with permission from Wiley

2.4 Stochastic Modelling and Predictive Simulation of Morphology and Functionality of Organic Semiconductor Materials at Various Length Scales

The focus of this section is on stochastic modelling and predictive simulation of the morphology of organic semiconductors and its coherence with functional properties of these materials like the dissociation efficiency of excitons at microscopic scale, or the mobility of charge carriers at molecular scale.

To begin with, morphological characteristics of microscopic image data of the underlying materials are computed using tools of stochastic geometry and spatial statistics [29]. Then, parametric stochastic morphology models are developed and the parameters are fitted to experimental data. Whenever a material can be produced using different processing parameters, the model can be fitted to a whole set of materials processed under different conditions, and a relation between processing parameters and model parameters can be found. This allows so-called predictive simulations, that is, creating virtual structures on the computer, which display processing parameters that have not been tested in the laboratory so far. Analysing the efficiency of those virtual materials is a much cheaper way to investigate the results of various processing parameters than creating those materials in the laboratory. Doing so, processing parameters can be optimized in order to improve functional properties of organic devices. This process is called virtual materials design.

In this section, stochastic morphology modelling and virtual materials design, which has been performed for three different types of materials, is discussed. In Subsection 2.4.1, hybrid polymer-ZnO solar cells (to be more precisely, P3HT:ZnO solar cells) are considered and their 3D morphology is described by a suitably chosen stochastic model. The model is fitted to various experimental data sets, which have been produced using different spin coating velocities. This makes it possible to use the model for predictive simulations for further spin coating velocities. Then, in Subsection 2.4.2, thin polymer:fullerene films (PDPP5T:$PC_{71}BM$ in a 1:2 ratio) are considered. This material is also produced using spin coating. A stochastic 2D model is fitted to TEM images of polymer:fullerene films produced with seven different spin coating velocities. The model accounts for the droplet-like fullerene parts in the films. Again, we perform regression in parameter space and show that the model is able to realize realistic morphologies for arbitrary spin coating velocities using cross validation. Finally, in Subsection 2.4.3, we briefly describe results which we obtained regarding morphological and electronic properties of networks of dicyanovinyl-substituted oligothiophene (DCV4T) molecules.

We also mention that in [30] we investigated the nanostructure of a further kind of organic–inorganic composites, which can be used as photoactive layers in hybrid–polymer solar cells. These materials consist of a polymeric (OC1C10-PPV) phase with CdSe nanoparticles embedded therein. On the basis of 3D image data with high spatial resolution, gained by electron tomography, an algorithm is developed in [30] to automatically extract the CdSe nanoparticles from grayscale images, where we assume them as spheres. The algorithm is based on a modified version of the Hough transform, where a watershed algorithm is used to separate the image data into basins such that each basin contains exactly one nanoparticle. Moreover, in [31], we applied techniques of spatial statistics for the characterization of the nanoscale 3D morphology of a hybrid solar cell based on a novel hierarchical nanostructured photoanode, where a cross section of the solar cell device has been prepared by focused ion beam milling in a micropillar geometry. This allows a detailed 3D reconstruction of the titania

photoanode by electron tomography. It turned out that the hierarchical titania nanostructure facilitates polymer infiltration, thus favouring intermixing of the two semiconducting phases, essential for charge separation. Again, the respective 3D nanoparticle network has been analysed with tools of stochastic geometry to extract information related to the charge transport in the hierarchical solar cell. In particular, the experimental dataset considered in [31] allows direct visualization of the percolation pathways that contribute to the photocurrent.

2.4.1. Hybrid Polymer ZnO Solar Cells

In this subsection, we consider the case of hybrid polymer-ZnO solar cells. In a first study [23], the relationship between 3D morphology and functionality of thin photoactive films of this type has been investigated by means of a descriptive statistical analysis, using electron tomography image data, see Fig. 2.9. This includes the analysis of spherical contact distances and percolation pathways as well as solving the three-dimensional exciton diffusion equation. Furthermore, in [26], the effect of side chain functionalization has been studied. Due to this analysis, a good understanding of the complex morphology could be gained. This knowledge has been used to develop a spatial stochastic model of the 3D morphology of hybrid polymer-ZnO solar cells, which has first been introduced in [32]. An overview with further mathematical background information can also be found in [33]. The stochastic morphology model is then used to perform virtual materials design and to analyse the resulting simulated 3D structures, see [34]. A more detailed analysis of the dependency between morphology and efficiency has been provided in [25]. In the following, the parametric morphology model of hybrid polymer-ZnO solar cells and the ideas of predictive simulation of such 3D morphologies for virtual materials design are described in more detail.

The stochastic morphology model is built on a multiscale approach to the representation of 3D image data, which has been introduced and applied to polymer solar cells in [35]. The basic idea is sketched in Fig. 2.12 (left). First, the binarized image is split in two parts – a morphologically smoothed one, representing the macro-scale morphology, and a second image containing structural details, which are referred to as micro-scale morphology, and are e.g. caused by thin ZnO-branches or isolated ZnO-particles. Both parts are modelled separately and combined to a stochastic model of the whole 3D structure.

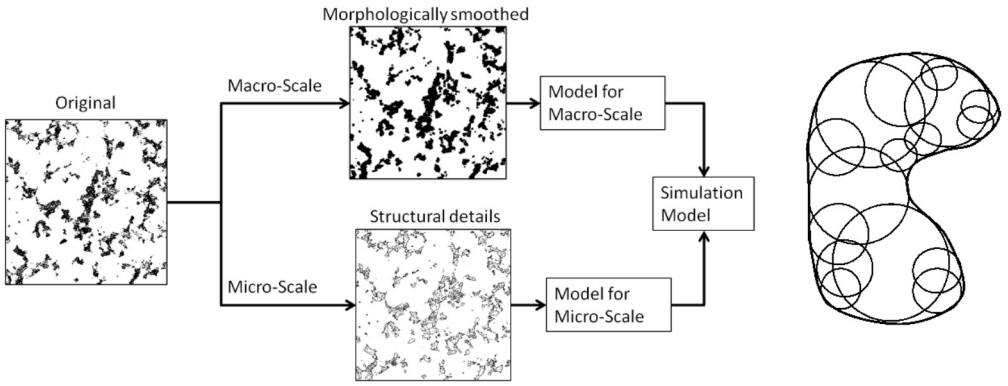

Fig. 2.12. Left: Distinction between macro- and micro-scale morphology; Right: Representation of ZnO phase by union of overlapping spheres. Reprinted from Ref. [35]

Modelling of the macro-scale morphology is based on a representation of the ZnO phase by a union of overlapping spheres, see Fig. 2.12 (right) for an illustrating planar section. This representation of the experimental data is achieved using an efficient stochastic segmentation algorithm, see [35] for details. Note that due to this representation, the macro-scale morphology can be interpreted as a marked point pattern, where the points are the midpoints of the spheres and the marks are the corresponding radii.

Modelling of such structures is possible using tools of stochastic geometry. In this particular case, the point pattern is modelled using a Markov chain of planar Poisson cluster processes, where clusters of points occur in ellipsoidal form and the centres of these clusters form a two-dimensional Poisson process, i.e., they do not interact with each other, but possess the property of complete spatial randomness (CSR). [32]. Given the point pattern, the radii are simulated. To account for the structure of the radii from the representation of the experimental data derived in [35], the distribution of radii and the so-called mark correlation function is analysed, where the mark correlation function of a marked point process describes the correlation of pairs of marks with a given distance of the corresponding points to each other. A positive correlation for small distances is observed. Therefore, radii are simulated using a so-called moving average procedure, where radii are first simulated independently of each other, using a gamma distribution. Note that the gamma distributions form a two-parameter family of continuous probability distributions, where the common exponential distribution and chi-squared distribution are special cases. Then to each point's mark the marks of a certain number of neighbouring points are added. This leads to a positive correlation of radii as desired. Furthermore, because the family of gamma distributions is closed with respect to convolution, the resulting distribution of radii is again gamma distributed, which fits to the observations in the experimental data. The whole simulation algorithm for the macro-scale morphology is summarized in Fig. 2.13.

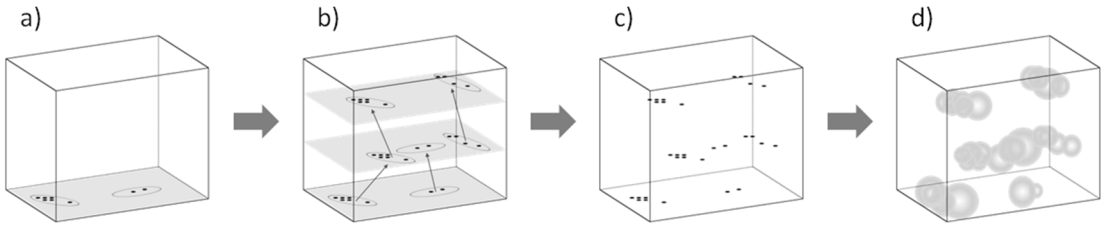

Fig. 2.13. Simulation algorithm. a) First 2D realization of cluster process. b) Markov chain of 2D cluster processes. c) Final point pattern. d) Final sphere system. Reprinted from Ref. [34] with permission from Wiley

Finally, the micro-scale morphology, which has been left out so far, is modelled given the macro-scale morphology. As an example, thin ZnO-branches and isolated ZnO-particles are simulated using marked Cox processes, which intensities and marks depend on the distance to the ZnO phase of the macro-scale morphology. Again, the marks correspond to the radii of respective spheres. Detailed information can be found in [32].

The model is fit to experimental data and validated using various morphological image characteristics. A good fit can be found, see [32] for details. In total, 6 different experimental data sets with different layer thicknesses have been considered, which result from different

spin coating velocities. The same model type can be fitted to all six data sets, and the parameter vector of the morphology model can be interpreted as a function of the spin coating velocity. This function is parametrized, such that using regression in the parameter space, predictive simulations for arbitrary spin coating velocities are possible. Doing so, virtual microstructures of polymer-ZnO solar cells can be simulated, which realistically mimic the dependence of the morphology on the spin coating velocity. For an impression of this dependence, see Fig. 2.14. The stochastic multiscale model is then used to create virtual 3D microstructures for a large number of spin coating velocities, which are subsequently analysed with respect to exciton dissociation efficiency and connectivity. It turns out that the microstructure tends to coarse with increasing spin coating velocity, where larger domains of polymer and ZnO are created. As a consequence, the exciton dissociation efficiency decreases significantly with increasing spin coating velocity.

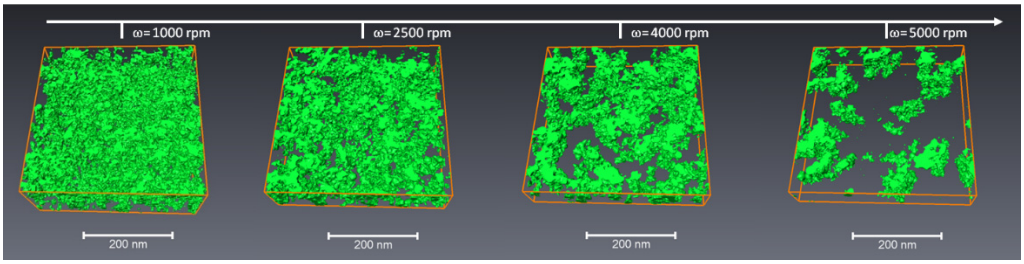

Fig. 2.14. Simulated realizations of the model for different spin coating velocities.

2.4.2 Polymer:Fullerene Semiconductor Films

We now turn to thin (50-500 nm) polymer:fullerene semiconductor films. In [28], tools of stochastic geometry and spatial statistics helped to correlate the dominant length scale of phase separation in this material to a normalized drying rate. Again, after comprehensive statistical analysis of the data, a parametric stochastic model has been developed, see [36].

The polymer:fullerene films consist of droplet-like fullerene agglomerates [28], which are called fullerene particles or simply particles in the following. The stochastic morphology model consists of three steps. First, the midpoints of fullerene particles are simulated using tools of point-process theory [29]. Then, based on the simulated point pattern, a so-called Voronoi tessellation is considered, which divides the space into disjoint cells, where each point generates exactly one cell. Note that a Voronoi cell consists of all those points which are closer to the generator point of the considered cell than to other generator points. Particles are simulated according to the size and shape of the cell corresponding to their midpoint. In the model, particles are either described by circles or the union of two overlapping circles, which fits to the shape of the particles observed in the experimental data. As a third step, a slight modification of particle positions is performed using a collective rearrangement algorithm. This is necessary to ensure a minimum distance between particles, as it is observed in the experimental data. An overview of the simulation algorithm is given in Fig. 2.15.

The model parameters are fitted to experimental data processed using seven different spin coating velocities. In each case, the model is determined by a surprisingly small number of parameters, but still describes the experimental data very well. This is seen from a good visual impression as well as morphological image analysis of experimental and simulated data, see [36] for details.

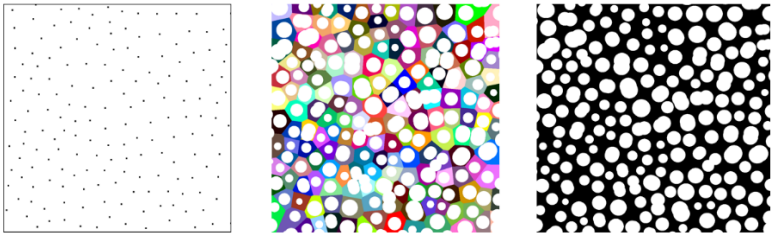

Fig. 2.15. Left: Point pattern of particle midpoints. Centre: Voronoi cells (coloured) and corresponding particles. Right: Final particle system after collective rearrangement

Due to the huge amount of different data sets, each of the model parameters could reliably be described as a function of spin coating velocity. This allowed us, as for the hybrid polymer-ZnO solar cells, to perform regression in the parameter space. In order to show the viability of this approach, we performed cross validation. We fitted the model only to six of the seven data sets, and used the information gained from that to estimate the model parameters for the seventh data set using the functional correlation between spin coating velocity and model parameters. Realizations using the model parameters estimated in that way were compared to the corresponding experimental data set, and a good coherence was found [36]. This approves that the model is able to capture the main morphological features of the thin polymer:fullerene films for arbitrary spin coating velocities.

2.4.3 Networks of DCV4T Molecules

In [37], we proposed a novel framework to study charge transport properties of materials via so-called random walkers in disordered random media. This framework combines a stochastic 3D model for the fast generation of random environments that realistically models material morphology with an algorithm for efficient estimation of key properties of the resulting random walk. This algorithm, called Aggregate Monte Carlo (AMC), was originally introduced in [38] and is a method for estimating the velocity of a random walker as it passes through a realization of the random environment, see also [39], where a prototype of the model to estimate charge carrier velocity in 1D is introduced. The algorithm works by first identifying and then aggregating problem regions in the random environment. We show that we are able to do this in such a way that our estimator is strongly consistent. Our stochastic morphology model represents the disordered medium as a random spatial graph with directed edge weights, where the edge weights represent the transition rates of a Markov jump process modelling the motion of the random walker and extends the spatial graph model introduced in [40]. It makes use of tools of spatial statistics and the theory of random geometric graphs. A particular strength is that it allows efficient simulation of large-scale molecular systems.

In particular, in [37] we describe our modelling framework by means of an example which illustrates an amorphous mesophase of an organic dye, used as an electron-donor in organic solar cells; see Fig. 2.16. Here, the random environment represents a molecular morphology, and the random walker describes the movement of a charge (hole) through the morphology. More specifically, we adjust the parameters of the model to the electronic properties of dicyanovinyl-substituted oligothiophene (DCV4T) molecules in a small (microscopic) system. The fitted model can be used to predict the mobility of holes in a morphology of DCV4T

molecules, see also [41]. Such a model can be of use for better understanding solar cells, as it allows for larger scale (experimentally relevant) modelling of such microscopic structures. For specific details on the microscopic simulation of DCV4T, we refer to [42,43].

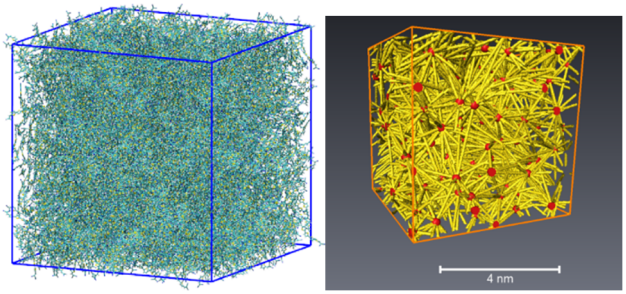

Fig. 2.16. Left: Large-scale morphology of DCV4T gained by microscopic simulations. Right: Corresponding 3D graph extracted from DCV4T morphology (cut-out), where vertices are displayed in red and edges are marked in yellow. Reprinted from Ref. [37] with permission from the Society for Industrial and Applied Mathematics

In the framework proposed in [37], the motion of the charge carrier is modelled using a Markov jump process, where the state space is a set of points. The transition probabilities depend on an underlying energy landscape, which is modelled using a Gaussian random field. Due to this procedure, there are regions with very low energy, in which the charge carrier becomes stuck, see Fig. 2.17 for a sketch. Therefore, the Monte Carlo estimation of charge carrier velocity has high variances and takes a lot of time. To reduce the number of simulation steps and decrease the variance, the ACM method is introduced which includes a coarsening of the state space based on a stochastic watershed algorithm.

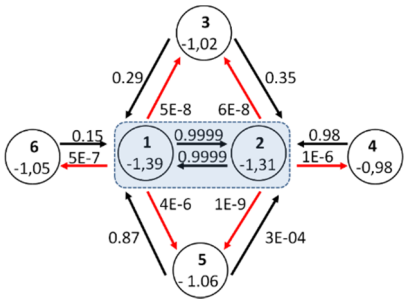

Fig. 2.17. Energy at different positions and corresponding transition probabilities. The carrier becomes stuck in the centre with very high probability. Reprinted with permission from Ref. [38] from Springer Science and Business Media

The stochastic approach presented in [37] is not limited to the particular organic semiconductor (DCV4T) we have used as a test system. In fact, the majority of host materials in organic light emitting diodes have large energetic disorder (deep traps) and are therefore challenging to model using small systems and the conventional variable step size method, see [44,45,46]. Modelling of network morphology using tools of stochastic geometry helps to increase the size of the system, while AMC provides an efficient way of evaluating its

properties, e.g., charge carrier mobility. Moreover, the developed techniques are not restricted to organic semiconductors. Similar problems are encountered, for example, when studying surface reactions (catalysis) [47] or hydrogen and oxygen transport in biological systems [48].

2.5 Conclusions

In this chapter we have addressed the design and synthesis of well-defined all-thiophene dendrons and dendrimers of different generations that can be functionalized at the periphery, in the branches and at the core with units that extend the absorption spectrum and influence the intermolecular interactions. These functionalized thiophene dendrimers were used to fabricate bulk heterojunction organic solar cells in which fullerenes acting as acceptor, reaching power conversion efficiencies up to 3%.

We further describe the relation between morphology and device performance using experimentally electron tomography data on polymer – metal oxide solar cells, using P3HT – ZnO an example. The remarkable increase in internal quantum efficiency and the device characteristics of the cells can be quantitatively described using a 3D electron-optical model that uses the actual nanometre scale morphology.

In the last section we have highlighted the use of stochastic methods for analysing the morphology of the polymer - metal oxide and polymer – fullerene bulk heterojunction blends. We have further shown that via the use of statistical models it is possible to create virtual blend morphologies that have the same characteristics as the experimentally determined bulk heterojunctions. Stochastic models have also been used to efficiently model charge transport in Monte Carlo simulations of device performance.

Acknowledgments

The authors would like to acknowledge the Deutsche Forschungsgemeinschaft in the framework of the DFG SPP1355, Collaborative Research Center 569 (SFB 569) for financial support. The authors acknowledge all the co-workers who actively participated in this research effort.

References

1 Y. Liu, J. Zhao, Z. Li, C. Mu, W. Ma, H. Hu, K. Jiang, H. Lin, H. Ade, H. Yan, Nat. Commun. **5**, 5293 (2014)
2 B. Kan, M. Li, Q. Zhang, F. Liu, X. Wan, Y. Wang, W. Ni, G. Long, X. Yang, H. Feng, Y. Zuo, M. Zhang, F. Huang, Y. Cao, T. P. Russell, Y. Chen, *J. Am. Chem. Soc.* **137**, 3886 (2015)
3 K. Müllen, G. Wegner (eds.), *Electronic Materials: The Oligomer Approach* (Wiley-VCH, Weinheim, 1998)
4 S. Gronowitz, A.-B. Hörnfeldt, *Thiophenes* (Elsevier Academic Press, San Diego, 2004)
5 J. S. Moore, Acc. Chem. Res. **30**, 402, (1997)
6 L. Gong, Q. Hu, L. Pu, J. Org. Chem. **66**, 2358 (2001)
7 S. K. Dev, T. M. Maddux, L. Yu, J. Am. Chem. Soc. **119**, 9079 (1997)

8 H. John, R. Bauer, P. Espindola, P. Sonar, J. Heinze, K. Müllen, Angew. Chem. Int. Ed. **44**, 2447 (2005)
9 A. J. Berresheim, M. Müller, K. Müllen, Chem. Rev. **99**, 1747 (1999)
10 C. Xia, X. Fan, J. Locklin, R. C. Advincula, Org. Lett. **4**, 2067 (2002)
11 C. Q. Ma, E. Mena-Osteritz, T. Debaerdemaeker, M. M. Wienk, R. A. Janssen, P. Bäuerle, Angew. Chem. Int. Ed. **46**, 1679 (2007)
12 C.-Q. Ma, M. Fonrodona, M. C. Schikora, M. M. Wienk, R. A. J. Janssen, P. Bäuerle, Adv. Funct. Mater. **18**, 3323 (2008)
13 C.-Q. Ma, E. Mena-Osteritz, M. Wunderlin, G. Schulz, P. Bäuerle, Chem.–Eur. J. **18**, 12880 (2012)
14 A. J. Mozer, C.-Q. Ma, W. W. H. Wong, D. J. Jones, P. Bäuerle, G. G. Wallace, Org. Electron. **11**, 573 (2010)
15 A. Mishra, C.-Q. Ma, R. A. J. Janssen, P. Bäuerle, Chem.–Eur. J. **15**, 13521 (2009)
16 W. W. H. Wong, C.-Q. Ma, W. Pisula, C. Yan, X. Feng, D. J. Jones, K. Müllen, R. A. J. Janssen, P. Bäuerle, A. B. Holmes, Chem. Mater. **22**, 457 (2010)
17 M. Mastalerz, V. Fischer, C.-Q. Ma, R. A. J. Janssen, P. Bäuerle, Org. Lett. 11, 4500 (2009)
18 G. L. Schulz, M. Mastalerz, C.-Q. Ma, M. Wienk, R. A. J. Janssen, P. Bäuerle, Macromolecules **46**, 2141 (2013)
19 M. K. R. Fischer, C.-Q. Ma, R. A. J. Janssen, T. Debaerdemaeker, P. Bäuerle, J. Mater. Chem. **19**, 4784 (2009)
20 M. K. R. Fischer, I. López-Duarte, M. M. Wienk, M. V. Martínez-Díaz, R. A. J. Janssen, P. Bäuerle, T. Torres, J. Am. Chem. Soc. **131**, 8669 (2009)
21 W.-S. Zhang, Dissertation, University of Ulm (2014)
22 L. J. A. Koster, M. Kemerink, M. M. Wienk, K. Máturova, R. A. J. Janssen, Adv. Mater. **23**, 1670 (2011)
23 S. D. Oosterhout, M. M. Wienk, S. S. van Bavel, R. Thiedmann, L. J. A. Koster, J. Gilot, J. Loos, V. Schmidt, R. A. J. Janssen, Nature Mater. **8**, 818 (2009)
24 L. J. A. Koster, Phys. Rev. B **81**, 205318 (2010)
25 L. J. A. Koster, O. Stenzel, S. D. Oosterhout, M. M. Wienk, V. Schmidt, R. A. J. Janssen, Adv. Energy Mater. **3**, 615 (2013)
26 S. D. Oosterhout, L. J. A. Koster, S. S. van Bavel, J. Loos, O. Stenzel, R. Thiedmann, V. Schmidt, B. Campo, T. J. Cleij, L. Lutzen, D. Vanderzande, M. M. Wienk, R. A. J. Janssen, Adv. Energy Mater. **1**, 90 (2011)
27 J. J. van Franeker, M. Turbiez, W. Li, M. M. Wienk, R. A. J. Janssen, Nat. Commum. **6**, 6229 (2015)
28 J. J. van Franeker, D. Westhoff, M. Turbiez, M. M. Wienk, V. Schmidt, R. A. J. Janssen, Adv. Funct. Mater. **25**, 855 (2015)
29 S. N. Chiu, D. Stoyan, W. S. Kendall, J. Mecke, *Stochastic Geometry and its Applications*. (J. Wiley & Sons, Chichester, 2013)
30 R. Thiedmann, A. Spettl, O. Stenzel, T. Zeibig, J. C. Hindson, Z. Saghi, N. C. Greenham, P. A. Midgley, V. Schmidt, Image Anal. Stereol. **31**, 23 (2012)
31 G. Divitini, O. Stenzel, A. Ghadirzadeh, S. Guarnera, V. Russo, C. S. Casari, A. L. Bassi, A. Petrozza, F. di Fonzo, V. Schmidt, C. Ducati, Adv. Funct. Mater. **24**, 3043 (2014)

32 O. Stenzel, H. Hassfeld, R. Thiedmann, L. J. A. Koster, S. D. Oosterhout, S. S. van Bavel, M. M. Wienk, J. Loos, R. A. J. Janssen, V. Schmidt, Ann. Appl. Stat. **5**, 1920 (2011)

33 V. Schmidt, G. Gaiselmann, O. Stenzel, in *Stochastic Geometry, Spatial Statistics and Random Fields: Models and Algorithms. Lecture Notes in Mathematics,* vol. 2120, ed. by V. Schmidt (Springer, Cham, 2015), p 95

34 O. Stenzel, L. J. A. Koster, R. Thiedmann, S. D. Oosterhout, R. A. J. Janssen, V. Schmidt, Adv. Funct. Mater. **22**, 1236 (2012)

35 R. Thiedmann, H. Hassfeld, O. Stenzel, L. J. A. Koster, S. D. Oosterhout, S. S. van Bavel, M. M. Wienk, J. Loos, R.A.J. Janssen, V. Schmidt, Image Anal. Stereol. **30**, 19 (2011)

36 D. Westhoff, J. J. van Franeker, T. Brereton, D. P. Kroese, R. A. J. Janssen, V. Schmidt, Modelling Simul. Mater. Sci. Eng. **23**, 045003 (2015)

37 O. Stenzel, C. Hirsch, T. Brereton, B. Baumeier, D. Andrienko, D. Kroese, V. Schmidt, Multiscale Model. Simul.,. **12**, 1108 (2014)

38 T. Brereton, O. Stenzel, B. Baumeier, D. Andrienko, V. Schmidt, D. P. Kroese, Methodol. Comput. Appl. Probab. **16**, 465 (2014)

39 T. J. Brereton, O. Stenzel, B. Baumeier, D. P. Kroese, V. Schmidt, in *Proceedings of the 2012 Winter Simulation Conference*, ed. by C. Laroque, J. Himmelspach, R. Pasupathy, O. Rose, A.M. Uhrmacher (IEEE, Piscataway, 2012)

40 B. Baumeier, O. Stenzel, C. Poelking, D. Andrienko, V. Schmidt, Phys. Rev. B **86**, 184202 (2012)

41 P. Kordt, O. Stenzel, B. Baumeier, V. Schmidt, D. Andrienko, J. Chem. Theory Comput. **10**, 2508 (2014)

42 M. Schrader, R. Fitzner, M. Hein, C. Elschner, B. Baumeier, M. Riede, K. Leo, P. Bäuerle, D. Andrienko, J. Am. Chem. Soc. **134**, 6052 (2012)

43 C. Elschner, M. Schrader, R. Fitzner, A. A. Levin, P. Bäuerle, D. Andrienko, K. Leo, M. Riede, RSC Adv. **3**, 12117 (2013)

44 V. Rühle, A. Lukyanov, F. May, M. Schrader, T. Vehoff, J. Kirkpatrick, B. Baumeier, D. Andrienko, J. Chem. Theory Comput. **7**, 3335 (2011)

45 F. May, M. Al-Helwi, B. Baumeier, W. Kowalsky, E. Fuchs, C. Lennartz, D. Andrienko, J. Am. Chem. Soc. **134**, 13818 (2012)

46 F. May, B. Baumeier, C. Lennartz, D. Andrienko, Phys. Rev. Lett. **109**, 136 (2012)

47 A.P.J. Jansen, *An Introduction to Kinetic Monte Carlo Simulations of Surface Reactions* (Springer, New York, 2012)

48 P. H. Wang, R. B. Best, J. Blumberger, J. Am. Chem. Soc. **133**, 3548 (2011)